metals

MDPI

Article

Numerical Modeling of the Influence of Nanometric Ceramic Particles on the Nucleation of AlSi10MnMg Alloy

Ane Jimenez [1,*], Jon Mikel Sanchez [1], Franck Girot [2,3], Mario Renderos [2] and Pedro Egizabal [1]

[1] TECNALIA, Basque Research and Technology Alliance (BRTA), Mikeletegi Pasealekua, 2, 20009 Donostia-San Sebastián, Spain; jonmikel.sanchez@tecnalia.com (J.M.S.); pedro.egizabal@tecnalia.com (P.E.)
[2] Department of Mechanical Engineering, Engineering School of Bizkaia, University of the Basque Country (UPV/EHU), Alameda de Urquijo s/n, 48013 Bilbao, Spain; frank.girot@ehu.eus (F.G.); marioalfredo.renderos@ehu.eus (M.R.)
[3] IKERBASQUE, Basque Foundation for Science, 48013 Bilbao, Spain
* Correspondence: ane.jimenez@tecnalia.com; Tel.: +34-667-10-25-43

Abstract: In recent years, many researchers have attempted to model the solidification process of nano-reinforced materials. In the present document, the effect on the heterogeneous solidification regime of the different sizes, shapes, and chemical compositions of nanometric ceramic particles in an AlSi10MnMg alloy is studied. This article develops a mathematical model to predict the solidification behavior of a general nano-reinforced alloy, then validates the results using experimental techniques. The main objective of the model is to minimize the costly and time-consuming experimental process of fabricating nano-reinforced alloys. The proposed model predicts the critical Gibbs energy and the critical radius required for nucleation in the heterogeneous solidification regime. Conversely, the experimental part focuses on understanding the solidification process from the differential thermal analysis (DTA) of the solidification curves. It was concluded that if subcooling is involved, cubic and pyramidal particles work better as nucleating particles in the studied alloy.

Keywords: heterogeneous solidification; modeling; shaped particles; mechanical properties; titanium carbide; alumina

Citation: Jimenez, A.; Sanchez, J.M.; Girot, F.; Renderos, M.; Egizabal, P. Numerical Modeling of the Influence of Nanometric Ceramic Particles on the Nucleation of AlSi10MnMg Alloy. *Metals* **2022**, *12*, 855. https://doi.org/10.3390/met12050855

Academic Editor: Frank Czerwinski

Received: 6 April 2022
Accepted: 13 May 2022
Published: 17 May 2022

1. Introduction

In the last few years, the automotive industry has promoted the development of lighter materials with better mechanical properties, seeking economic, environmental, and political benefits. Therefore, research is needed on the improvement of lighter materials as a way to lower fuel consumption, which will enable a drop in pollutant gas emissions [1]. One way to meet this challenge is to introduce ceramic nanoparticles into a lightweight alloy to modify the final microstructure of the material, with the purpose of improving its mechanical properties [2,3]. To achieve improvement in the mechanical properties of metal materials i.e., strength and ductility, nanometric particles have proven to be a feasible approach for obtaining the required result [4].

The process used to improve the mechanical properties of the aluminum alloy consists of introducing nanometric particles into the material before casting so that the particles act as solidification germs of the α-Al phase. By locating the nanoparticles in this phase, two of the relevant mechanical properties, i.e., the strength and the ductility, can be enhanced due to the grain refinement of the microstructure. Therefore, it is necessary to quantify how much the incorporated nanoparticles can act as heterogeneous solidification germs. Among the factors that most influence the effectiveness of the particles are their size, shape, and surface properties [5,6].

In metallic alloys, the nucleation process is understood as the beginning of a phase transformation in a small region [7,8]. In this process, atoms come together and organize

themselves to move from the liquid phase to a solid phase. For the nucleation process to occur, small embryos must first form. As these embryos reach the critical radius, they will tend to form a stable nucleus, which grows to create a crystal. Otherwise, the atoms or molecules separate, dissolving back into the liquid. Based on the model that other researchers have developed for the study of nucleation from spherical particles, it was considered desirable to study the effect of introducing differently shaped particles, i.e., cubic and pyramidal forms [9,10]. Currently, with the boom in the development of new nanoparticle-reinforced alloys using particles of different geometries, it is interesting to extend the spherical model to other shapes, such as cubes and pyramids. The influence of geometry on heterogeneous germination has yet to be properly understood. In earlier studies, a framework for modeling coupled nucleation, growth, and coarsening in diluted alloys, based on different methods, has been developed [11–16].

In the present work, with the aim of understanding the influence of introducing different ceramic particles into a liquid aluminum alloy, a model for different particle shapes and sizes has been developed. With the model, the critical Gibbs energies for each reinforced alloy can be obtained so that spherical, cubic, and pyramidal particles can be compared. In cases in which the needed energy for nucleation is less than that of the homogeneous material, the particles are going to behave as a solidification germ. Moreover, the influence of introducing nanoparticles on the solidification curve has been studied, for which DTA has been carried out. In the case of spherical and cubic nanoparticles, the mathematical model is validated using experimental results. In the case of pyramidal particles, only the mathematical model is shown. The experimental development was performed on two different samples of AlSi10MnMg alloy, one of them alloyed with cubic TiC and the other with spherical Al_2O_3 ceramic nanoparticles. The developed mathematical models predict the critical Gibbs energy and the critical radius that the nuclei must achieve to initiate stable nucleation. The model allows predicting nucleation behavior as a function of the shape, size, and chemical composition of the introduced particles.

2. Materials and Methods

The Thermo-Calc software (v. 2020, Thermo-Calc Software AB, Stockholm, Sweden) was used in conjunction with the TCAL7 thermodynamic database to calculate the non-equilibrium solidification properties of the alloys [17]. The AlSi10MnMg ingots were melted in a silicon carbide crucible, heated in an electric resistance furnace that can hold up to 3 kg of aluminum alloy. The stir-casting process [18] was used to introduce the nanometric ceramic particles to the AlSi10MnMg alloy. The process consisted of melting the aluminum, raising the furnace temperature to 710–740 °C; once the material was melted, the stirrer was introduced to generate a vortex. To ensure the proper agitation of the alloy, the stirrer remained centered. In this work, particles of two different shapes and compositions (Al_2O_3 and TiC) were compared. In both cases, the size of the nanoparticles (equivalent diameter) was 80 nm. The nanoparticles were introduced to the molten alloy and, to ensure their homogeneous distribution, the stirring was maintained for 15 min. Finally, the melted mixture was cooled down to 700–720 °C and poured into a steel mold preheated to 100 °C. Before casting, samples were poured into standard QuiK-Cup® sand cups. The dataset for DTA was collected using a high-speed National Instruments® data acquisition system.

3. Results and Discussion

3.1. Compositional Analysis

The elemental composition of the molten bath was analyzed using optical emission spectrometry (OES); the results are shown in Table 1. It should be noted that in the case of the alloy reinforced with Al_2O_3 (Base + Al_2O_3), the chemical composition is quite similar to that of the base alloy. This is due to the fact that the spectrometer is not capable of detecting aluminum oxides in an aluminum base alloy.

Table 1. Elemental composition (in wt %) of the molten alloys obtained by OES.

Ref.	Al	Fe	Si	Mn	Cr	Ni	Zn	Mg	Ti	Sr	V
Base	Bal.	0.16	10.92	0.55	0.01	0.01	0.01	0.24	0.05	0.01	0.01
Base + TiC	Bal.	0.19	11.31	0.54	0.01	0.01	0.01	0.25	0.10	0.01	0.01
Base + Al_2O_3	Bal.	0.17	11.12	0.54	0.01	0.01	0.01	0.24	0.05	0.01	0.01

3.2. Heterogeneous Solidification Model for Nano-Metric Particles

In this work, the developed mathematical model analyses the phase transformation of the aluminum by studying the Gibbs energy, which allows the prediction of the critical radius needed to start the phase transformation from liquid to solid [7].

The model that has been developed is based on the known equation for the homogeneous scenario, in which the free energy of the homogenous surface (ΔG_{hom}) can be expressed as:

$$\Delta G_{hom} = V \cdot \Delta G_v + A_s \cdot \gamma \quad (1)$$

where V is the volume of the nuclei, ΔG_v is the volumetric Gibbs energy difference, A_s is the superficial area of the nuclei, and γ is the surface tension. Moreover, according to the third law of thermodynamics, the volumetric Gibbs energy can be expressed as [19]:

$$\Delta G_v = \Delta H_v - T \cdot \Delta S \quad (2)$$

where ΔG_v is the volumetric Gibbs energy, T is the phase transformation temperature, ΔH_v is the increase in enthalpy of the system, and ΔS is the increase in entropy of the system.

Considering that in the vicinity of the melting temperature, the liquid and solid states coexist, the volumetric Gibbs energy difference can be expressed as:

$$\Delta G_v = \frac{\Delta T \cdot \Delta H_v}{T_m} \quad (3)$$

where ΔT is the difference between the melting and phase transformation temperatures. Considering the mathematical deduction, the critical radius r^* for the homogeneous solidification case can be calculated as follows:

$$r^*_{hom} = -\frac{2\gamma}{\Delta G_v} \quad (4)$$

For this specific radius, Gibbs energy can be expressed as:

$$\Delta G^*_{hom} = \frac{16\pi \cdot \gamma^3}{{\Delta G_v}^2} \left(\frac{T_m}{\Delta T \cdot \Delta H_v} \right) \quad (5)$$

Once the formulation and the methodology used for the homogeneous case are known, in the heterogeneous nucleation model, it is assumed that nucleation occurs when the nucleus forms on impurities or on the walls of the vessel containing the liquid. When the melt contains solid particles, or they form from simple contact with the crucible wall or an oxide layer, the probability of the nucleation of small nuclei increases, even with a small number of atoms, i.e., the activation energy required for the formation of a stable nucleus decreases. In this work, based on the shape of the introduced nanoparticles, there are three case studies for heterogeneous nucleation (spherical, cubic, and pyramidal), in which the critical radius equation is obtained from the derivative of the Gibbs energy equation since the critical radius coincides with the point at which the maximum energy is reached.

3.2.1. Spherical Particles

Figure 1 shows the schematic illustration of a scenario in which the reinforcing particles have a spherical shape.

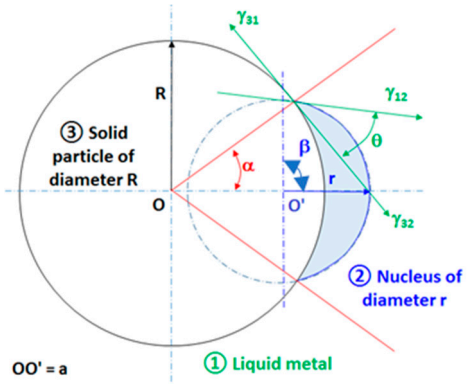

Where the surfaces S are:

$$S_{12} = 2\pi r^2(1 - cos\beta),$$

$$S_{23} = 2\pi R^2(1 - cos\alpha) \text{ and}$$

$$V = \frac{\pi}{3}[r^3(1 - cos\beta)^2(2 + cos\beta) - R^3(1 - cos\alpha)^2(2 + cos\alpha)]$$

Figure 1. Schematic illustration of the spherical particle nucleation.

Considering the mathematical relationships obtained from Figure 1, in which θ is the wettability angle [20], in the case of spherical particles, the Gibbs energy of the system (ΔG_{sph}) is defined as:

$$\Delta G_{sph} = \Delta G_V \cdot V + \gamma_{12} \cdot S_{12} + (\gamma_{23} - \gamma_{13})\, S_{23} \quad (6)$$

where γ_{12} is the contact angle between the nuclei and the liquid metal, γ_{23} is the contact angle between the nuclei and the spherical particle, S_{12} is the surface of the nucleus in contact with the liquid, and S_{23} is the surface of the nucleus in contact with the spherical nanoparticle.

3.2.2. Cubic Particles with a Nucleus on One Face

Figure 2a shows the schematic illustration of the scenario in which the reinforcing particles have a cubic shape. In the case of cubic particles, the nucleation occurs on one face of the cube, as shown in Figure 2b. The critical radius and Gibbs energy are obtained by imposing the condition of a constant wetting angle.

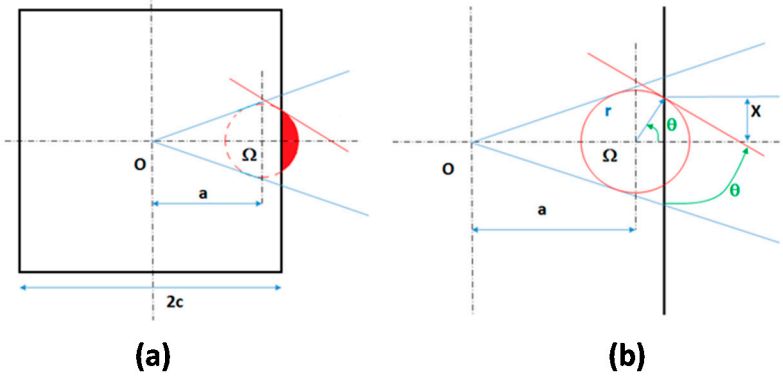

Figure 2. (**a**) Schematic illustration of cubic particles with the nucleus on one face, and (**b**) the detailed section of the formation of the nucleus from the face of a cubic particle.

In the mathematical modeling of the cubic particles, the length of the cubic particle was defined as "2c", the distance between the center of the cubic particle and the center of the nuclei was defined as "a", the coordinate of the circumference inscribing the cap of the growing nucleus was defined as Ω, and the radius of the cap on the face of the nucleating particle was defined as X.

3.2.3. Cubic Particles with a Nucleus on the Vertex

Figures 3 and 4 show the schematic illustration of diferent possible cases in which the reinforcing particles have a cubic shape with a nucleus on the vertex, so that, the nucleus has developed on a corner of the particle. To keep the wettability angle constant, it assumed

that the center of the particle moves towards the inside or outside of the cube. Due to geometrical reasons, the minimum wetting angle is 45° (Figure 3b). Therefore, for lower angle values (Figure 3a), the preferential nucleation will be on the face of the cube.

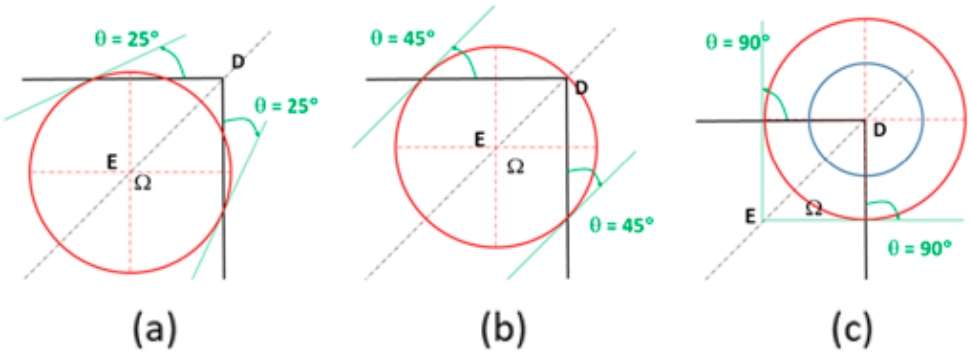

Figure 3. Scheme of the critical wettability angles, with a nucleus on the vertex of a cubic particle. (**a**) Case for $\theta < 45°$. (**b**) Case for $\theta = 45°$. (**c**) Case for $\theta > 45°$.

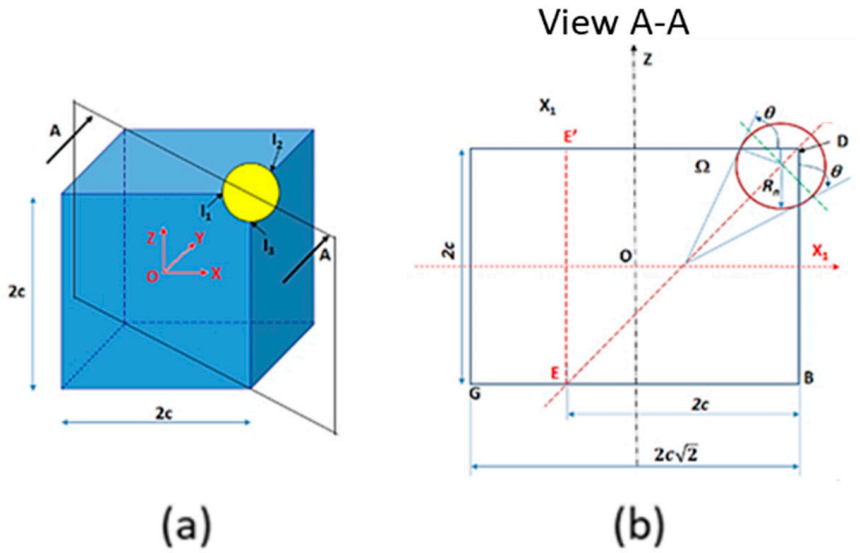

Figure 4. Schematic illustration of cubic particles with a nucleus on the vertex. (**a**) Perspective view of nucleus growth in the corner of the cubic particle; (**b**) Section view (A-A) for the geometric derivation of model volumes and surfaces for this section.

In Figure 3c, the center of the nucleus and the corner of the cube (D) are the same and the grains grew centered at the corner. As done in the previous cases, the Gibbs energy will be obtained from the ratio of angles, contact surfaces, and volumes.

3.2.4. Pyramidal Particles

Figure 5 shows the schematic illustration of the pyramidal particles; the length of the pyramidal particle was defined as "a". Considering the formed spherical cap, the Girard theorem was applied [21]. Following this theorem, if α, β, and γ are the measures in radians of the angles of the spherical triangle ABC, on a sphere of radius r, the area of this spherical triangle is equal to $(\alpha + \beta + \gamma - \pi)\, r^2$. This assumption was taken into consideration to calculate the Gibbs energy equation for the system.

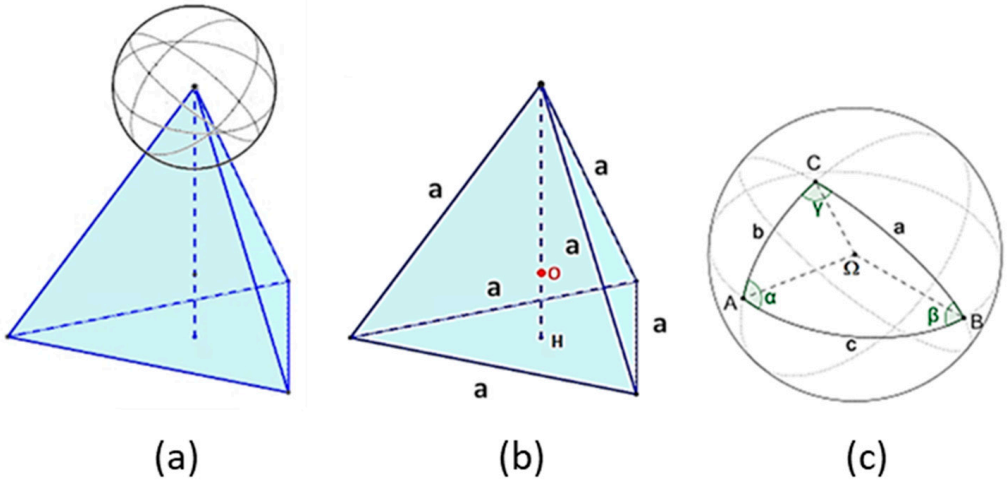

Figure 5. Schematic illustration of the nuclei grows in a pyramidal particle. (**a**) The nucleus growing, (**b**) the shape of the particle, and (**c**) spherical cap shape detail.

3.2.5. Numerical Modeling

To obtain the equations to predict the critical Gibbs energy of each scenario, the volumes and contact surfaces were obtained and substituted into Equation (1). In Table 2, the values for the studied cubic and pyramidal cases are summarized. These values were obtained in a similar way to the prediction made for the spherical particles.

Table 2. Calculated volume and contact surface in the function of the particle shape.

Particle Shape	Volume	Contact Surface
Cubic, with a nucleus on one face	$V = \frac{\pi}{3}\, r^3 \cdot (2 + cos(\theta)) \cdot (1 - cos(\theta))^2$	$S_{12} = 2\pi\, r^2 \cdot (1 - cos(\theta))$ $S_{23} = \pi\, r^2 \cdot cos(\theta)^2$
Cubic, with a nucleus on the vertex $\theta \geq 45°$	$V = \frac{4\pi}{3}\, r^3 \cdot h_1(\theta)$	$S_{12} = 4\pi\, r^2\, h_2(\theta)$ $S_{23} = \frac{3r^2}{2} h_3(\theta)$
Pyramidal	$V = \frac{4\pi}{3} r^3 - \frac{\sqrt{2}}{12} r^3$	$S_{12} = \left[5\pi - 3 \cdot arcos\left(\frac{1}{3}\right)\right] \cdot r^2$ $S_{23} = 3 \cdot \frac{\sqrt{3}}{4} \cdot r^2$

Here, for a cubic particle with a nucleus on the vertex, $h_n(\theta) = a_n + b_n\, cos\theta + c_n cos^2$, as follows:

n	a	b	c
1	0.8815967897	−0.654080314	−0.5033064535
2	0.8665609048	−0.276518036	−0.4422067834
3	0.3570758524	0.7369844695	1.179334371

The developed mathematical relationships of the critical Gibbs energy and form factor in the function of the particle shape are summarized in Table 3. These equations were obtained from the geometries shown in Figures 1–5 and follow the methodology previously detailed in the case of spherical particles.

Figure 6 shows the difference in the Gibbs energy curve due to the introduction of TiC and Al_2O_3 nanoparticles. In the case studied, it was assumed that the wetting angle between these particles and the AlSi10MnMg alloy was $\theta = 90°$. Regarding particle shape, note that: (1) TiC nanoparticles are cubic, and (2) Al_2O_3 nanoparticles are spherical. In both cases, the particles used have an approximate size of 80 nm (equivalent diameter).

Table 3. Calculated critical Gibbs energy and form factor in the function of the particle shape.

Particle Shape	Critical Gibbs Energy	Form Factor
Spherical	$\Delta G^*_{sph} = \frac{16\pi\gamma_{12}^3}{3\Delta G_v^2} \cdot F_{sph}(m,x)$	$F_{sph}(m,x) = \frac{1}{2}\left\{1-\left(\frac{mx-1}{g}\right)^3 + x^3\left[2-3\left(\frac{x-m}{g}\right)+\left(\frac{x-m}{g}\right)^3\right] + 3mx^2\left(\frac{x-m}{g}-1\right)\right\}$ being $g = \sqrt{1+x^2-2mx}$ and $x = R/r^*$; $m = cos\theta$
Cubic, with a nucleus on one face	$\Delta G^*_{c:face} = \frac{16\pi\gamma_{12}^3}{3\Delta G_v^2} \cdot F_{c:face}(\theta)$	$F_{c;face}(\theta) = f(\theta) = \frac{1}{4}\left(2-3cos\theta+cos^3\theta\right)$
Cubic, with a nucleus on the vertex $\theta \geq 45°$	$\Delta G^*_{c:vertex} = \frac{16\pi\gamma_{12}^3}{3\Delta G_v^2} \cdot F_{c:vertex}(\theta)$	$F_{c:vertex}(\theta) = 3\left[\frac{-1}{12} f_{cu:vertex}(\theta)\cdot h_1(\theta) + h_2(\theta) - \frac{3}{8}h_3(\theta)\cdot cos\theta\right]\cdot f^2_{c:vertex}(\theta)$
Pyramidal	$\Delta G^*_{pyramidal} = \frac{16\pi\gamma_{12}^3}{3\Delta G_v^2} \cdot F_{pyramidal}(\theta)$	$F_{pyramidal}(\theta) = \frac{\sqrt{2}\left(8\sqrt{2}\pi-1\right)}{16\pi} \cdot f^3_{pyramidal}(\theta)$

Here $f_{c:vertex}(\theta) = \frac{8\cdot h_2(\theta)-3h_3(\theta)\cdot cos\theta}{8\cdot h_1(\theta)}$ *and* $f_{pyramidal}(\theta) = \frac{\sqrt{2}\left[12atan\left(\frac{\sqrt{2}}{2}\right)-\pi(cos\theta+10)\right]}{1-8\sqrt{2}\pi}$.

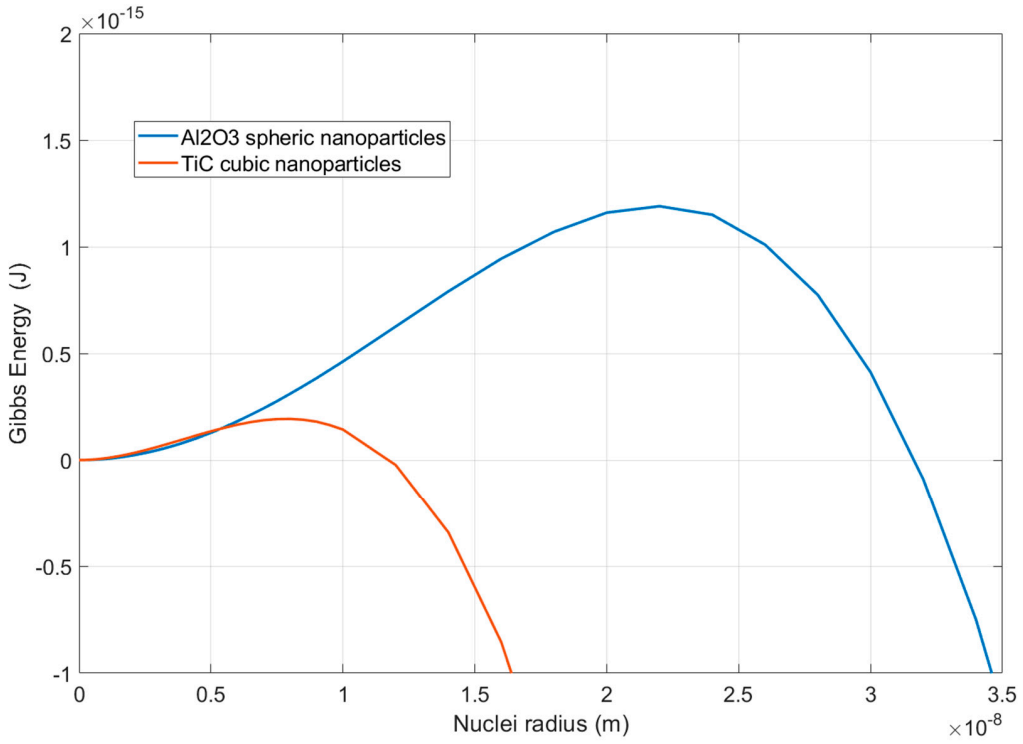

Figure 6. Influence of the introduction of TiC and Al_2O_3 nanoparticles on the Gibbs energy.

As can be seen from the previous Figure 6, at a similar particle volume, cubic particles are more favorable for heterogeneous solidification than spherical particles. Based on the form factors shown in Table 3, the same effect was obtained with a pyramidal particle.

3.3. Influence of the Nanometric Particles in the Solidification Properties of the Alloys

Figure 7 shows the non-equilibrium solidification curve of the AlSi10MnMg (base alloy). The calculation was performed using the Thermo-Calc software, using the elemental composition obtained in Table 1. In the diagram, three different curves are plotted, obtained with the classic Scheil model (Scheil calculator 1), the Scheil model with back diffusion in the primary phase (Scheil Calculator 2), and the equilibrium model (dotted line).

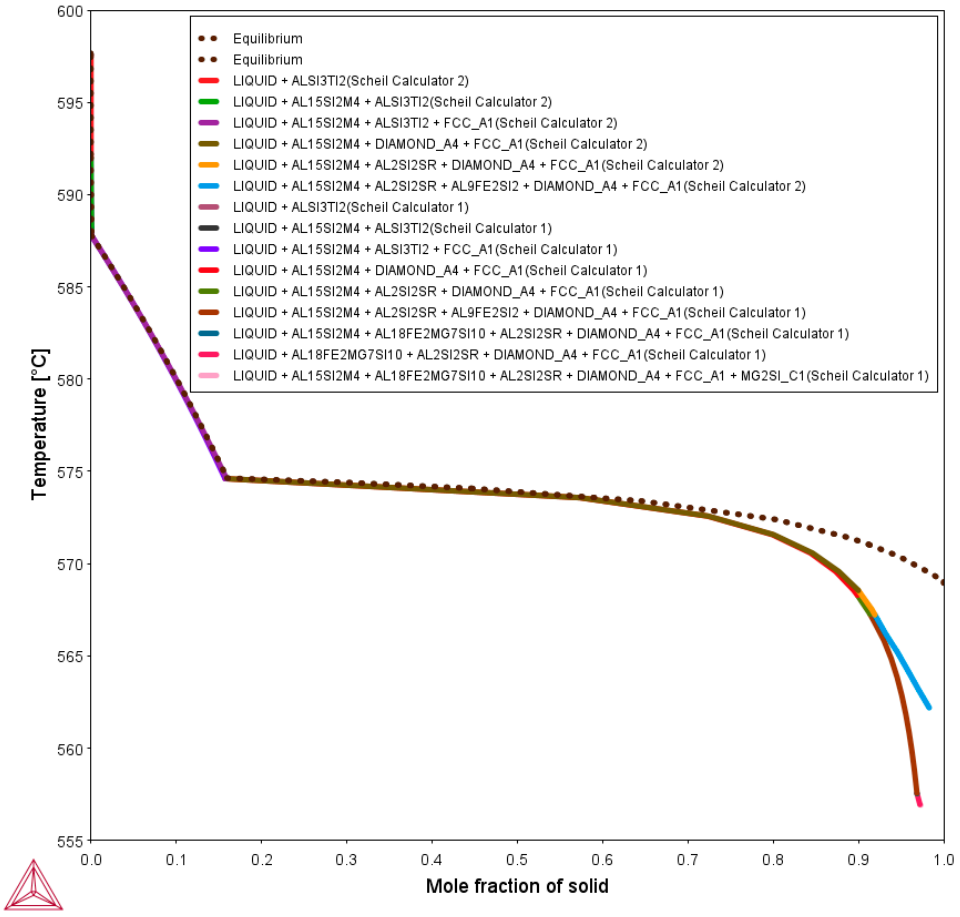

Figure 7. Non-equilibrium solidification curves of AlSi10MnMg alloy, obtained using different solidification models.

The input data of the Scheil model with back diffusion had a cooling rate of 0.2 °C/s and a secondary dendrite arm-spacing of 20 µm. The data were experimentally obtained via DTA and image analysis. As the nucleation of the nanometric ceramic particles occurred during the first stages of solidification, an analysis of the cooling curves in the first stages of solidification was conducted. All the curves exhibited the same solidification pattern when the temperature was over 572 °C. The liquidus point was at 598 °C in all the curves. At this temperature, the $AlSi_3Ti_2$ compound was precipitated from the liquid phase. At 592 °C, the $Al_{15}Si_2(Mn,Fe,Cr)_4$ phase was precipitated. Then, when the temperature cooled down to 588 °C, the precipitation of the α-Al phase was initiated. At 574 °C, a sharp downturn was observed in the curves. This is correlated with the precipitation of the eutectic Si particles. The equilibrium model (dotted line) diverged from the other ones when the Si phase was stabilized; this divergence was more visible at 573 °C. After this temperature, the solidification path of this model was completely different from the other ones.

Therefore, the non-equilibrium solidification sequence of AlSi10MnMg at the beginning of the solidification is as follows:

- Liquid (L)→ L + $AlSi_3Ti_2$ at 598 °C
- L + $AlSi_3Ti_2$ + $Al_{15}Si(Mn,Fe)_4$ at 591 °C
- L + $AlSi_3Ti_2$ + $Al_{15}Si(Mn,Fe)_4$ + α-Al at 588 °C
- L + $AlSi_3Ti_2$ + $Al_{15}Si(Mn,Fe)_4$ + α-Al + Si at 575 °C

As can be seen, in the base alloy, there are only two compounds that promote the refinement of the microstructure, the $AlSi_3Ti_2$ and $Al_{15}Si(Mn,Fe)_4$ intermetallic phases. These phases can be clearly distinguished in the non-equilibrium solidification curves (Figure 7), as they present an almost vertical line shape.

The experimental solidification properties of the alloys studied were obtained by means of DTA of the solidification curves, using the first and second derivatives of the phase-change curves. As an example, in Figure 8, the cooling curve and the first derivative of AlSi10MnMg (base alloy) are represented. The pouring temperature (T_p), liquidus temperature (T_L), and the temperature precipitation of the Al-Si eutectic ($T_{\text{Al-Si}}$) and solidus temperature (T_{Sol}) were also marked in the curve.

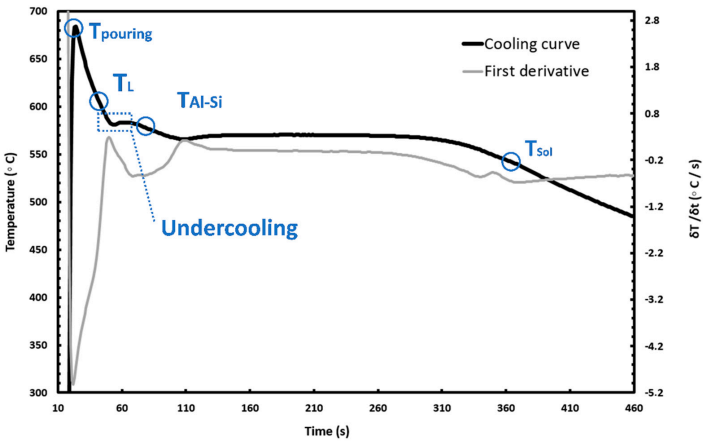

Figure 8. The cooling curve and the first derivative dT/dt of AlSi10MnMg alloy.

In Figure 9, the section of the solidification curve related to the undercooling is highlighted. From the previous figure, it is possible to determine the effectiveness of the added particles in terms of heterogeneous nucleation and, therefore, grain refinement. This is performed by analyzing the cooling curve in detail (Figure 9). The behavior of the cooling curve in the highlighted section gives a good indication of the effect of particle introduction on the solidification of the alloy [17]. It is well known that the curves exhibit little undercooling when many nucleating particles are present. It is also assumed that if there are few nucleating particles, there will be less undercooling. Therefore, the subcooling parameter (ΔT) can be calculated using the following equation:

$$\Delta T = T_G - T_M \tag{7}$$

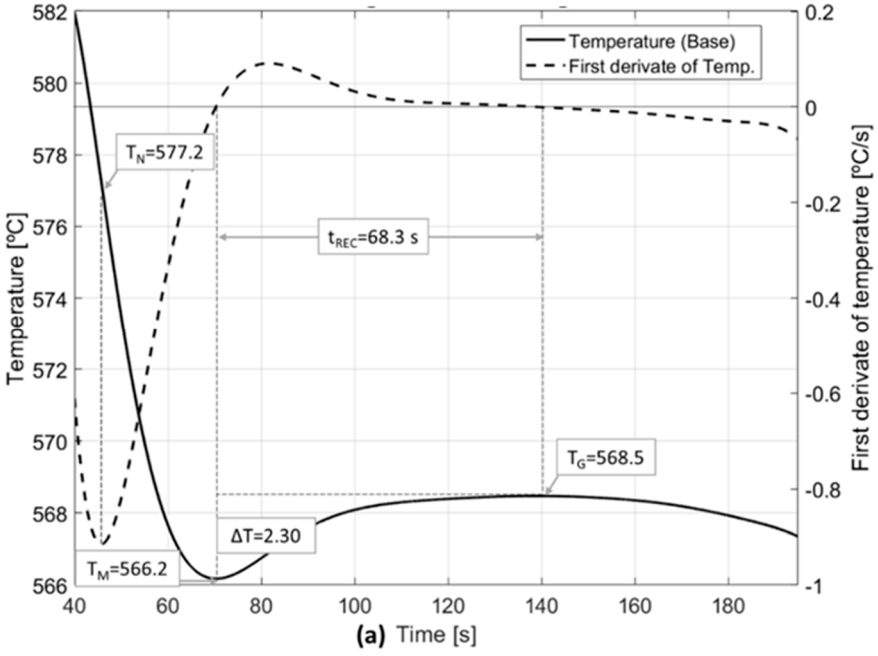

Figure 9. *Cont.*

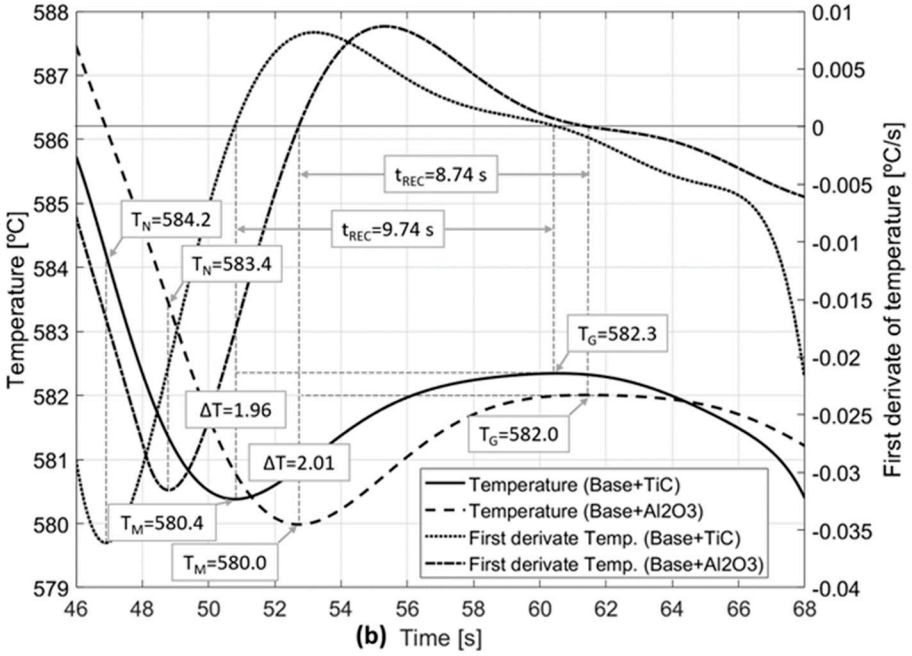

Figure 9. Cooling curves in the range of undercooling of (**a**) base alloy and (**b**) base + TiC and base + Al_2O_3 alloys.

The following parameters representative of undercooling are defined, thus: (T_M) is the temperature at which newly nucleated crystals have grown to such an extent that the released latent heat goes out of equilibrium; (T_G) represents the steady-state growth temperature of the molten metal; (T_N) is the start of the nucleation temperature, the nucleation power of the particles present in the liquid metal. These previous parameters are most easily recognized by a sudden change in the first derivative, as shown in Figure 9a. The period required for this heating is called the recalescence period (t_{REC}). After this time, the molten metal heats up to the steady-state growth temperature.

The above-mentioned solidification properties of the studied alloys are summarized in Table 4. In terms of the effectiveness of the particles, it is observed that the introduction of the Al_2O_3 and TiC nanoparticles promotes a decrease in the undercooling parameter. Furthermore, the TiC nanoparticles proved to be more effective.

Table 4. Solidification properties of the studied alloys.

Calculation	Liquidus (°C)	$T_{Al\text{-}Si}$ (°C)	T_N (°C)	T_G (°C)	T_M (°C)	ΔT (°C)	t_{REC} (s)
Thermo-Calc	597	575	-	-	-	-	-
Base	598	576	577.2	568.5	566.2	2.3	68.35
Base + Al_2O_3	590	577	583.4	582.0	580.0	2.0	8.74
Base + TiC	591	578	584.2	582.3	580.4	1.9	9.74

4. Conclusions

With the aim of understanding the effect of introducing different ceramic particles into a liquid aluminum alloy, a model for different particle shapes with a size of 80 nm has been developed. TiC and Al_2O_3 nanoparticles were incorporated in an AlSi10MnMg alloy. The model for heterogeneous solidification, when applied to spherical, cubic, and pyramidal particles, allows comparison of the efficiency of different types of particles to improve the behavior of TiC. Furthermore, based on the form factor obtained (Table 3), it is concluded that for heterogeneous nucleation to be favorable, the introduced particles must be spherical or cubic. In the case of cubic particles, nucleation will occur on one face

of the particle. Otherwise, the shape factor obtained is greater than 1, which implies that the particles do not have the tendency to act as a solidification germ.

To verify the conclusions obtained from the model, a detailed analysis of the solidification DTA curve in the subcooling zone was carried out, and the beneficial effect of the particles was validated and compared. The nanoparticles added to AlSi10MnMg act as a grain refiner, even if they do not have the effectiveness of the TiB_2 particles commonly used for refining (ΔT of the order of 0.1 to 0.2 °C) [22]. However, this improvement verifies the correct incorporation of the nanoparticles into the primary α-aluminum phase.

For the AlSi10MnMg base alloy, the nucleation of the first germs takes place at a temperature, T_N, lower than the growth temperature, T_G. However, in cases where the alloy has been reinforced with nanoparticles, that nucleation temperature is higher than the growth temperature, proof of a certain refining by those particles. Furthermore, the undercooling value ΔT decreases (almost 0.4° for 80 nm TiC particles) and the growth temperature T_G rises and approaches the equilibrium temperature, T_E.

For a similar size, considering the critical temperatures obtained for each case, TiC is slightly more efficient than Al_2O_3. This is related to the fact that TiC, as TiB_2, helps to refine the grain of aluminum alloys [22].

Author Contributions: Conceptualization, A.J.; formal analysis, J.M.S. and M.R.; funding acquisition, P.E.; investigation, J.M.S., M.R., A.J. and F.G.; methodology, P.E.; project administration, P.E.; resources, P.E.; supervision F.G.; validation, F.G. and P.E.; writing—original draft, A.J.; writing—review and editing, J.M.S. and M.R. All authors have read and agreed to the published version of the manuscript.

Funding: This work was supported by project ICME—Methodology for multi-scale process-microstructure-properties-performance modelling for the improvement of the design of materials, processes and components in the metal industry of the Basque Country. ICME project has received funding from the Basque Government under the ELKARTEK Program (KK-2021/00022).

Institutional Review Board Statement: Not applicable.

Informed Consent Statement: Not applicable.

Data Availability Statement: Not applicable.

Conflicts of Interest: The authors declare no conflict of interest.

References

1. Koli, D.K.; Agnihotri, G.; Purohit, R. Advanced Aluminium Matrix Composites: The Critical Need of Auto-motive and Aerospace Engineering Fields. *Mater. Today Proc.* **2015**, *2*, 3032–3041. [CrossRef]
2. Lazarova, R.; Bojanova, N.; Dimitrova, R.; Panov, I.; Manolov, V. Influence of Nanoparticles Introducing in the Melt of Aluminum Alloys on Castings Microstructure and Properties. *Int. J. Met.* **2016**, *10*, 466–476. [CrossRef]
3. Zhukov, I.A.; Kozulin, A.A.; Khrustalyov, A.P.; Kahidze, N.I.; Khmeleva, M.G.; Moskvichev, E.N.; Lychagin, D.V.; Vorozhtsov, A.B. Pure Aluminum Structure and Mechanical Properties Modified by Al2O3 Nanoparticles and Ultrasonic Treatment. *Metals* **2019**, *9*, 1199. [CrossRef]
4. Nishida, Y. *Introduction to Metal Matrix Composites: Fabrication and Recycling*; Springer: New York, NY, USA, 2013.
5. Sajjadi, S.; Ezatpour, H.; Parizi, M.T. Comparison of microstructure and mechanical properties of A356 aluminum alloy/Al_2O_3 composites fabricated by stir and compo-casting processes. *Mater. Des.* **2012**, *34*, 106–111. [CrossRef]
6. Hamedan, A.D.; Shahmiri, M. Production of A356–1wt% SiC nanocomposite by the modified stir casting method. *Mater. Sci. Eng. A* **2012**, *556*, 921–926. [CrossRef]
7. Mahata, A.; Zaeem, M.A.; Baskes, M.I. Understanding homogeneous nucleation in solidification of aluminum by molecular dynamics simulations. *Model. Simul. Mater. Sci. Eng.* **2018**, *26*, 025007. [CrossRef]
8. Nicolas, M.; Deschamps, A. Characterisation and modelling of precipitate evolution in an Al–Zn–Mg alloy during non-isothermal heat treatments. *Acta Mater.* **2003**, *51*, 6077–6094. [CrossRef]
9. Qian, M. Heterogeneous nucleation on potent spherical substrates during solidification. *Acta Mater.* **2006**, *55*, 943–953. [CrossRef]
10. Stefanescu, D.M. *Science and Engineering of Casting Solidification*; Springer: Cham, Switzerland, 2015.
11. Myhr, O.R.; Grong, Ø. Modelling of non-isothermal transformations in alloys containing a particle distribution. *Acta Mater.* **2000**, *48*, 1605–1615. [CrossRef]
12. Perez, M.; Dumont, M.; Acevedo-Reyes, D. Implementation of classical nucleation and growth theories for precipitation. *Acta Mater.* **2008**, *56*, 2119–2132. [CrossRef]

13. Kampmann, R.; Wagner, R. Chapter Kinetics of precipitation in metastable binary alloys—Theory and application to Cu-1.9 at% Ti and Ni-14 at% Al. In *Decomposition of Alloys: The Early Stages*; Haasen, P., Gerold, V., Wagner, R., Ashby, Y.M.F., Eds.; Pergamon: Sonnenbergm, Germany, 1984; pp. 91–103. [CrossRef]
14. Oxtoby, D.W. Nucleation of Crystals from the Melt. *Adv. Chem. Phys.* **1988**, *70*, 263–296. [CrossRef]
15. Vehkamäki, H.; Määttänen, A.; Lauri, A.; Napari, I.; Kulmala, M. Technical Note: The heterogeneous Zeldovich factor. *Atmos. Chem. Phys.* **2007**, *7*, 309–313. [CrossRef]
16. Kolmasiak, C.; Łągiewka, M. Solidification of the Al alloy composite reinforced with graphite particles. *Metalurgija* **2021**, *60*, 399–402.
17. Andersson, J.-O.; Helander, T.; Höglund, L.; Shi, P.; Sundman, B. Thermo-Calc & DICTRA, computational tools for materials science. *Calphad* **2002**, *26*, 273–312. [CrossRef]
18. Mosisa, E.; Bazhin, V.Y.; Savchenkov, Y.S. Review on nano particle reinforced aluminum metal matrix compo-sites. *J. Appl. Sci. Res.* **2016**, *11*, 188–196. [CrossRef]
19. Sunyaev, R.A. (Ed.) On the Theory of New Phase Formation. Cavitation. In *Selected Works of Yakov Borisovich Zeldovich, Volume I: Chemical Physics and Hydrodynanics*; Princeton University Press: Princeton, NJ, USA, 2014; pp. 120–137. [CrossRef]
20. Bracco, G.; Holst, B. (Eds.) *Surface Science Techniques: 51*; Springer: Berlin/Heidelberg, Germany, 2013.
21. Karliga, B.; Tokeser, U. Girard Type Theorems for de Sitter Triangles with non-null Edges. *arXiv* **2017**, arXiv:1412.5507.
22. Backenrud, L.; Krol, E.; Tamminem, J. *Solidification Characteristics of Aluminium Alloys*; American Foundrymans Society/Skanaluminium: Oslo, Norway, 1990; Volume 2.